scientific reports

Check for updates

OPEN

Size-Dependent Wetting Contact Angles at the Nanoscale Defined by Equimolar Surfaces and Surfaces of Tension

Sergii Burian[1,5]✉, Yevhenii Shportun[1], Andriy Yaroshchuk[2,3], Leonid Bulavin[1], David Lacroix[4] & Mykola Isaiev[4]

The wetting characteristics of fluids play a crucial role in various fields of interface and surface science. Contact angle serves as a fundamental indicator of wetting behavior. However, accurate quantification of wetting phenomena even at the macroscale often poses challenges, particularly due to the hysteresis between receding and advancing contact angles. The complexity increases further at the nanoscale, where the significant volume of the interphase region causes ambiguity in defining the "dividing surface." In this study, we use molecular dynamics simulations to investigate the wetting dynamics of a "cylindrical nanodroplet" and an argon nanofilm. Through analysis of microscopic density distribution maps and tension tensor distributions within the Gibbs framework, we identified equimolar and tension surfaces at both liquid-gas and liquid-solid interfaces. Our results show over 10% discrepancies between equilibrium contact angles calculated for equimolar surfaces and those based on tension surfaces in the case of the cylindrical nanodroplet. We observed a clear dependence of wetting contact angles on the cross-sectional radius of cylindrical droplets with a straight three-phase contact line. As the radius decreases, the differences between contact angles at equimolar and tension surfaces increase, while for larger droplets, these differences diminish and become negligible.

Keywords Wetting, Nanodroplet, Surface tension, Wetting contact angle, Tolman length

Wetting phenomena stand out as one of the most captivating aspects in various scientific and industrial domains. Despite a rich exploration history, the spreading of a liquid over a solid surface still requires investigation through interdisciplinary approaches, particularly due to its multiscale nature[1]. Understanding wetting phenomena has been a gradual process marked by several well-known milestones and breakthroughs[2]. Among the most significant milestones in understanding wetting phenomena are Young's equation, which describes the equilibrium of forces at the contact line; the influence of surface morphology as captured by the Cassie-Baxter and Wenzel models; and the phenomenon of contact angle hysteresis[3], which reflects the difference between advancing and receding contact angles. As we examine to the tiniest scales, we begin to see the emergence of complex phenomena, with the effects of size-dependent surface tension and line tension becoming increasingly important[4–6].

In this context, several open questions remain. For instance, until now, a consensus concerning the magnitude and sign of the "Tolman length", a parameter describing the size dependence of surface tension, has yet to be reached even for the simplest case of a spherical droplet[7]. There are several fundamental works[8,9]and well-known monographs[10,11]arguing that the surface tension should decrease with the reduction of the droplet radius. However, an opposite viewpoint can also be found in both earlier[12,13]and more recent works[14–21]. Additionally, as demonstrated in[21] the surface tension of water for droplets increases as their size decreases, whereas for bubbles, the surface tension decreases with a reduction in bubble size. Droplets and bubbles exhibit different rates of change in surface tension.

In the work[22]Gurkov and Kralchevsky pointed out that for interfaces with low surface tension (for example, micro-emulsions), the thermodynamic surface of tension could be located far away from the transitional zone

[1]Faculty of Physics, Taras Shevchenko National University of Kyiv, 64/13, Volodymyrska Street, Kyiv 01601, Ukraine. [2]ICREA, Barcelona 08010, Spain. [3]Department of Chemical Engineering, Universitat Politècnica de Catalunya, Barcelona 08028, Spain. [4]Faculté des Sciences et Technologies, LEMTA – Université de Lorraine – CNRS UMR 7563, Boîte Postale 70239, Vandoeuvre les Nancy cedex 54506, France. [5]Department of Macrokinetics natural disperse systems, F.D. Ovcharenko Institute of Biocolloidal Chemistry, Kyiv 03142, Ukraine. ✉email: burian_sergii@knu.ua

of division between the adjacent phases. They also noted that in this case, it would be more appropriate to use different dividing surfaces, distinct from the surface of tension. When considering the boundaries of three phases, this may necessitate revising the concept of the "Wetting Contact Angle" (WCA). Indeed, the WCA is one of the key characteristics of wetting phenomenon[2]. Usually[23–25], the WCA is determined at each point along the three-phase contact line, where the WCA is represented as a dihedral angle formed by the intersection of two tangent planes at the interfaces of two adjacent phases (liquid-solid and liquid-gas) With macroscopic objects, the thickness of interphase regions is negligibly small in comparison with its characteristic linear dimensions, such as the radius of curvature of the dividing surface. Therefore, within the resolution of measuring instruments, the position of the dividing surface of macroscopic systems is uniquely defined. Thus, it can be assumed that the dividing surface is completely matching with the interphase region. As a consequence, the determination of the dividing surface position of the macroscopic physical bodies does not cause significant difficulties and mainly is a technical task[23].

However, in real physical systems, the properties of adjacent homogeneous thermodynamic phases do not change abruptly, but gradually, i.e., the density and components of the pressure tensor change smoothly within a transition region that always has some finite thickness and volume[26,27]. At the same time, the characteristic dimensions of nanoscale objects can be comparable to the transition region thickness. This gives rise to fundamental difficulties in attempting to uniquely determine the position of the dividing surface as a mathematical surface of zero thickness. Therefore, it is essential to consider the context when defining the dividing surface in nanoscale systems, distinguishing it from the transition region between adjacent phases of the thermodynamic system.

In the literature, several methods have been proposed to define the position of dividing surfaces at the liquid-gas and liquid-solid interfaces. These methods can sometimes produce ambiguous results. For example, in computer simulation studies, the iso-density surface is often used as the dividing surface between phases in one-component systems. The density is calculated using various approaches. For instance, a study[28] selected several iso-density lines, approximated by circles, and assumed that the wetting angle is the average angle between different iso-surfaces. In the work by Weijs et al.[29], they assumed that line tension does not affect the shape of a sessile droplet's upper part. This shape resembles a cylindrical segment with uniform density. They concluded that the contact angle should match Young's macroscopic equation. This condition applies when the surface density equals half the bulk density of the liquid phase. Other researchers, such as Hong-Kai and Hai-Ping[30], propose that the dividing surface is located where the density is half of the liquid-phase density. Ingebretsen and Toxvaerd[31] determine the dividing surface position by fitting the density profile with empirical formulas using the densities of liquid and gas phases. To determine the WCA, they use the difference in the position of the Gibbs dividing surfaces, focusing on the two layers closest to the solid surface.

Another issue is the strong oscillations in the density of sessile droplets at the surface of solid substrates. These oscillations cause distortions in the iso-density surfaces, deviating from the ideal cylindrical or spherical shapes. To minimize the impact of these oscillations, most authors exclude parts of the droplet with strong density fluctuations from their analyses. Instead, they focus on the sections with more stable densities. The approximation is typically limited to the substrate, but the WCA can also be measured at different heights above the substrate. For example, in[32], the authors measure the WCA directly at the substrate's surface. In another study, the WCA is calculated at a distance corresponding to half the characteristic interaction distance from the top row of substrate atoms[31]. Yamaguchi et al.[33] also determine the WCA at the boundary of the solid substrate and the first adsorption layer, where the density of the droplet's liquid sharply increases from a zero. This corresponds to the nearest boundary the liquid molecules can reach during thermal motion.

Indeed, the use of Gibbs dividing-surface method is much simpler because there is no need to specify the microscopic behavior of the density profiles and the local values of the pressure tensor components in the interphase region[26]. To determine the equilibrium WCA, the position of the equimolar dividing surface and the surface of tension are defined using Gibbs approach. This is an extension of the thermodynamic method of the Gibbs dividing surfaces, where the use of surface of tension ensures the full mechanical equivalence between the reference and real systems (see works of Kralchevsky[34,35]). Since the thermodynamic equilibrium of heterogeneous systems, apart from thermal and chemical equilibria, also implies mechanical equilibrium, it is appropriate to use the surface of tension for calculating WCA. Therefore, it is proposed that the contact angle should be understood as a dihedral angle at the three-phase line of tension between surfaces that are tangential to the respective surfaces of tension.

Methodology for calculating the position of dividing surfaces

Calculating the position of the surface of tension often more efficient when using a combined approach involving the Tolman length, δ. This length is defined as the difference between the positions of the equimolar dividing surface (radius R_e) and the surface of tension:

$$\delta = R_e - R \tag{1}$$

The approach we propose here involves indirectly calculating the position of the surface of tension by utilizing the micromechanical approach[36]. Specifically, we define it as the position of the equimolar surface adjusted by the Tolman length δ:

$$R = R_e - \delta \tag{2}$$

In the case of a free surface of tension[21], determining the Tolman length δ is relatively straightforward. However, for a sessile droplet, this calculation becomes significantly more complex. Nevertheless, it has been

established[37–39]that the Tolman length weakly depends on the curvature of the surface of tension, allowing its determination for a flat surface of a thin film at the liquid-gas boundary of the same substance and temperature, particularly given the significant temperature dependence of the Tolman length[21]. For the model systems studied here, a key feature of the equimolar surface is that its position, within the systematic error of MD calculations, closely aligns with the contour where the density equals half of the volumetric density of the liquid phase. Consequently, the position of the equimolar surface can be accurately determined if one of its main sections is known to have the shape of a circular arc.

For an arbitrarily curved dividing surface, the Gibbs adsorption is calculated using this formula[40]:

$$\Gamma = \int_{\lambda^{\alpha}}^{\lambda^{\beta}} \left(n(\lambda) - n^{\alpha\beta}\right)\left(1 + \lambda J + \lambda^2 K\right) d\lambda, \tag{3}$$

where $J = c_1 + c_2$ and $K = c_1 c_2$are the Euler and Gaussian curvatures respectively, λ^{α} and λ^{β} are such that $n(\lambda^{\alpha}) = n^{\alpha}$ and $n\left(\lambda^{\beta}\right) = n^{\beta}$, and the function $n^{\alpha\beta} = \left\{n^{\alpha},\ \lambda < 0;\ n^{\beta},\ \lambda > 0\right\}$.

In the case of weakly curved surfaces, that is, those whose thickness is significantly less than the radius of curvature of the dividing surface ($\lambda^{\beta} - \lambda^{\alpha} \ll R$) when substituting variables in the integral of expression (3):

$$R + \lambda = z; \qquad R + \lambda^{\alpha} = Z_{\alpha}; \qquad R + \lambda^{\beta} = Z_{\beta}, \tag{4}$$

the same expression is obtained as for calculating adsorption in the case of a flat dividing surface of a single-component two-phase system:

$$\Gamma(Z) = \int_{Z_{\alpha}}^{Z} \left(n(z) - n^{\alpha}\right) dz + \int_{Z}^{Z_{\beta}} \left(n(z) - n^{\beta}\right) dz, \tag{5}$$

where $\Gamma(Z)$ is the adsorption calculated for the dividing surface at the point with coordinate Z, $n(z)$ is the substance concentration of the real system at the point with coordinate z, n^{α} is the equilibrium concentration of the liquid phase of the reference system, n^{β} is the equilibrium concentration of its vapor phase, Z_{α} is the coordinate corresponding to the point in space where the concentration becomes equal to the bulk concentration of the liquid phase $n(Z_{\alpha}) = n^{\alpha}$, and Z_{β} is the space coordinate where the concentration is equal to the bulk concentration of the vapor phase, $n(Z_{\beta}) = n^{\beta}$.

The position of the equimolar dividing surface Z_e is determined from the condition of zero adsorption $\Gamma(Z)$ on the left side of equation (5), that is, by setting $\Gamma(Z_e) = 0$. By rearranging the terms on its right side, and integration by parts, the following convenient expression is obtained:

$$Z_e = \frac{1}{n^{\beta} - n^{\alpha}} \int_{Z_{\alpha}}^{Z_{\beta}} z \frac{\partial n(z)}{\partial z} dz, \tag{6}$$

To determine the location of the curved surface of tension Z_s, it is customary to use expressions for the thermodynamic surface tension and shear energy:

$$\gamma = -\frac{1}{2}\int_{\lambda^{\alpha}}^{\lambda^{\beta}} \widehat{\boldsymbol{I}}_S : \widehat{\boldsymbol{P}}^S \chi\, d\lambda; \qquad \zeta = -\frac{1}{2}\int_{\lambda^{\alpha}}^{\lambda^{\beta}} \widehat{\boldsymbol{q}} : \widehat{\boldsymbol{P}}^S \chi\, d\lambda, \tag{7}$$

Similar mechanical quantities are found using the formulas:

$$\sigma = -\frac{1}{2}\int_{\lambda^{\alpha}}^{\lambda^{\beta}} \widehat{\boldsymbol{L}} : \widehat{\boldsymbol{P}}^S d\lambda; \qquad \eta = -\frac{1}{2}\int_{\lambda^{\alpha}}^{\lambda^{\beta}} \left(\widehat{\boldsymbol{q}} \cdot \widehat{\boldsymbol{L}}\right) : \widehat{\boldsymbol{P}}^S d\lambda, \tag{8}$$

where the auxiliary coefficients χ and $\widehat{\boldsymbol{L}}$, whose meaning is detailed in the works[41,42], are defined by the following expressions: $\chi = (1 - \lambda H)^2 - \lambda^2 D^2$, $\widehat{\boldsymbol{L}} = (1 - 2\lambda H)\widehat{\boldsymbol{I}}_S + \lambda \widehat{\boldsymbol{b}}$. The values H and D represent the mean and differential curvatures, respectively, and are defined in terms of the principal curvatures c_1 and c_2: $H = (c_1 + c_2)/2$, $D = (c_1 - c_2)/2$. These parameters describe the shape and curvature of the phase interface. For the surface of tension, the tensors $\widehat{\boldsymbol{I}}_S$ and $\widehat{\boldsymbol{b}}$ are mutually orthogonal but do not form a complete set of basis tensors. The curvature tensor $\widehat{\boldsymbol{b}}$ can be expressed as a linear combination of these tensors, and it is decomposed into its trace $H\widehat{\boldsymbol{I}}_S$ and deviator $D\widehat{\boldsymbol{q}}$, as shown in the equation: $\widehat{\boldsymbol{b}} = H\widehat{\boldsymbol{I}}_S + D\widehat{\boldsymbol{q}}$. Thus, determining the position of the surface of tension requires accounting for these curvatures, ensuring accurate modeling of the mechanical and thermodynamic properties in the interfacial region between phases.

In the case of flat phase-dividing surfaces, the expressions for micromechanical determination of surface tension coincide for thermodynamic (7) and mechanical (8) surface tensions coincide, and with the substitution of variables (4) and considering the approximation $\lambda^{\beta} - \lambda^{\alpha} \ll R$, they can be transformed into Bakker's formula[43], which is usually used to calculate the surface tension $\gamma_{\alpha\beta}$ at the flat boundaries between adjacent phases:

$$\gamma_{\alpha\beta} = \int_{Z^{\alpha}}^{Z^{\beta}} (P_N - P_T)\, dz, \tag{9}$$

where $P_N = P_N(z)$ and $P_T = P_T(z)$ are the normal and tangential components of the pressure tensor in the real system, respectively. The condition for the equality of the momentum of force acting on an elementary cross-section that normally intersects the interphase region in the real system and the momentum of force acting on a similar cross-section in the reference system:

$$\gamma_{\alpha\beta} Z_s = \int_{Z^{\alpha}}^{Z^{\beta}} (P_N - P_T)\, z dz. \tag{10}$$

Considering expressions (9) and (10), Z_s is determined by the formula:

$$Z_s = \int_{Z^{\alpha}}^{Z^{\beta}} (P_N - P_T)\, z dz \Big/ \int_{Z^{\alpha}}^{Z^{\beta}} (P_N - P_T)\, dz. \tag{11}$$

Similar to expression (1), the difference between Z_e and Z_s is the Tolman length δ:

$$\delta = Z_e - Z_s. \tag{12}$$

MD calculations of argon nanofilms and nanodroplets

To investigate the wetting characteristics and the size dependence of the contact angle, we modeled nanodroplets of various sizes placed on an ideal solid substrate in equilibrium with the vapor of the same liquid as the droplet. To eliminate the influence of the curved three-phase contact line, we selected droplets in the shape of cylindrical segments, which also simplified the procedure for calculating density profiles and pressure tensor components. To better understand the behavior of the substance in the interfacial region without edge effects, we also modeled a nanofilm that wets the same substrate as the droplet and is in equilibrium with its saturated vapor.

To avoid the necessity of making additional assumptions regarding combining rules[44], such as Berthelot-Lorentz rules concerning the interaction of atoms of different types in molecular dynamics calculations, we employed a single-component system of argon atoms[45]. This choice allowed us to set the simulation temperature to the triple point of argon (83.8058 K), where solid, liquid, and vapor phases coexist, thus accurately representing the equilibrium conditions of the system. This choice was crucial for studying the contact angle of wetting.

For multicomponent systems where interactions between different types of atoms or molecules must be considered, traditional combining rules, such as the Berthelot-Lorentz rules, may introduce certain inaccuracies, especially at the nanoscale. However, as demonstrated in our previous work[46], it is possible to apply an alternative method for adjusting the potential parameters for interactions between the fluid and the solid substrate. This approach allows for accurate adjustment of interaction parameters based on macroscopic wetting measurements, which provides an adequate representation of interfacial properties without the need for additional assumptions regarding combining rules. This method can be successfully used for more complex multicomponent systems, such as water or other fluids.

The MD simulations were performed using the LAMMPS (Large-scale Atomic/Molecular Massively Parallel Simulator) package[47]. The argon fluid was modeled in mechanical and chemical equilibrium with its saturated vapor, with the equilibrium maintained by an external inhomogeneous force field that simulated the substrate (see further in the text Eq. (13) and (S1) see Supplementary Material, Section A.). Given that we used a canonical ensemble (NVT), the pressure was not directly controlled but instead emerged naturally from the system's equilibration process. The Gibbs canonical ensemble was selected for molecular dynamics modeling as it simplifies the MD calculations of the profiles of density and pressure-tensor components by maintaining constant volume and temperature throughout the simulation.

To ensure the accuracy of these simulations, particular attention was given to modeling the substrate, as it plays a critical role in the interaction dynamics of the nanodroplets and nanofilms with their surrounding environment.

Modeling of the substrate

To accelerate the MD simulations, the substrate was modeled using the time-averaged force field that it would generate in space at the triple-point temperature, as described by the potential in Eq. (S1) (see Supplementary Material, Section A. for details[32,48,49]). At this temperature, the numerical density of solid argon was assumed to be approximately 0.021357 $Å^{-3}$.

Due to specific technical requirements of the MD simulations, the potential well depth was set at two lattice periods from the bottom wall of the simulation box. The resulting potential is illustrated in Fig. 1 (a):

$$\Phi(z) = \frac{2}{3}\pi n \sigma^3 \epsilon \left(\frac{2}{15} \frac{\sigma^9}{\left(z - \left(2a_0 - (2/5)^{1/6}\right)\sigma\right)^9} - \frac{\sigma^3}{\left(z - \left(2a_0 - (2/5)^{1/6}\right)\sigma\right)^3} \right) \tag{13}$$

where $n = \sqrt{2} a_0^{-3}$, and a_0, the crystal lattice period for argon, was estimated as 5.25 Å, σ = 3.405 Å. The parameter ϵ was used to control the degree of wettability of the substrate, its values were chosen to be 80%,

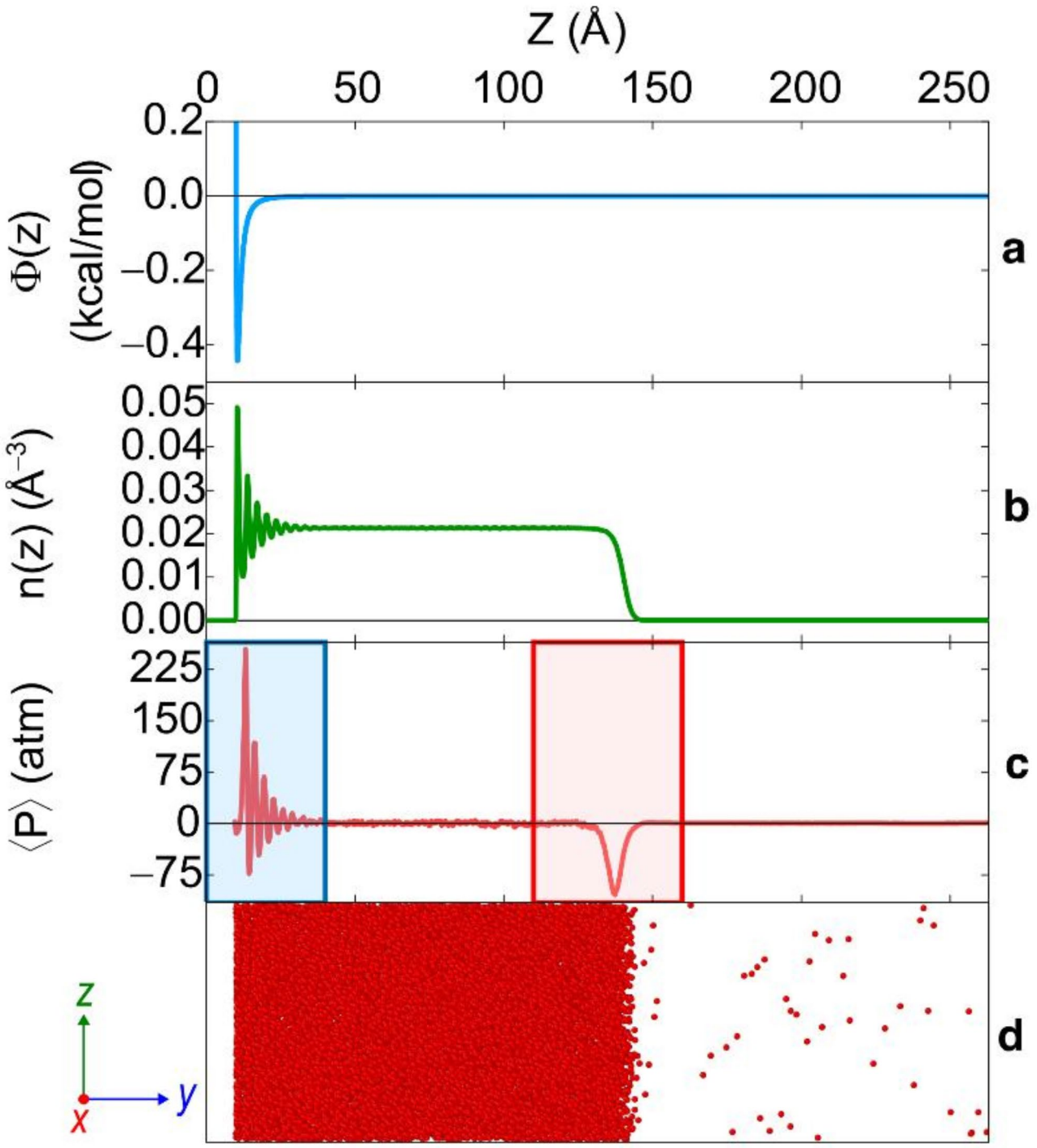

Fig. 1. To facilitate analysis, we plot the wall potential Φ(z) (Eq. (13)) (**a**), with energy expressed in kcal/mol, a specific unit of measurement used for the simulation (thermochemical kilocalories, i.e., 1 cal∘= 4.184 J). This means that the corresponding energy in kilocalories must be divided by Avogadro's constant. (**b**) The distribution of numerical density values $n(z)$ along the z-direction, averaged over the x- and y-directions during 5 ns of the simulation. (**c**) The average hydrostatic pressure $\langle P(z) \rangle$ of the vapor-liquid system. The rectangular areas highlighted in (c) are further detailed in Figs. S4 and S5 (see Supplementary Material, Section C. Modeling of the argon nanofilm for details). (**d**) Schematic representation of the argon nanofilm atoms' position in the thermalized configuration after reaching equilibrium at a temperature of 83.8058 K.

100%, and 120% of 1.032 meV to simulate varying degrees of surface interaction. For a detailed mathematical derivation of the potential field, refer to the supplementary material (see Section A. Modeling of the substrate).

Modeling of the argon nanofilm

This subsection presents the results of the MD simulations of the wetting phenomenon by an argon nanofilm on a virtual solid substrate, represented by a wall potential (13) that mimics the interactions at the solid-liquid interface.

Simulation setup

For the simulation of the nanofilm, a simulation box with dimensions of $78.75 \times 78.75 \times 262.5$ Å^3 and with periodic boundary conditions in two directions tangent to the film surface (x, y) and boundary conditions corresponding to mirror reflection in the z-direction was considered. In the initial configuration, argon atoms were created at the nodes of a face-centered cubic lattice, which had a period of 5.25 Å, and filled part of the space of the simulation box with dimensions $73.5 \times 73.5 \times 52.5$ Å^3. As a result, the model vapor-liquid system comprised 17,241 argon atoms (see Fig. 1.).

The interaction of argon atoms was modeled using the Lennard-Jones potential with the following parameters: $\sigma = 3.405$ and $\epsilon = 1.032$ meV. Therefore, all the computer simulation results presented in this study, involving MD modeling of argon vapor-liquid systems, were conducted with a cut-off radius of the interparticle potential equal to 10σ. The justification for selecting this cut-off radius is provided in the supplementary material (see in Supplementary Material, Section B. Choice of the cut-off radius for the interparticle potential (see Ono and Kondo[11] and De Groot & Mazur[50]).

To reach equilibrium, the system was heated from 1 K to the triple point temperature during 1 ns and thermalized for 6 ns. The resulting thermalized configuration allowed us to proceed with the analysis of the wetting behavior of the argon nanofilm under equilibrium conditions.

The numerical integration of Newton's equations in the MD simulations was performed using the velocity Verlet al.gorithm with a time step of 1 fs. For the argon nanofilm, two-dimensional maps of numerical density distribution, components of the mechanical stress tensor, and Voronoi diagrams[51] were averaged over values generated every 100 steps during 1 ns, with the total simulation time lasting 10 ns.

Calculation of the surface tension and Tolman length

To determine the Tolman length (12) in the case of a flat interface, the positions of the equimolar dividing surface and the surface of tension are first calculated using expressions (6) and (11) respectively. The positions of the equimolar surface and the surface of tension were determined using formulas (6) and (11), respectively. The equimolar surface position was calculated based on the density distribution along the normal to the interface, as demonstrated in the density profiles shown in Figures S2 and S3 (see Supplementary Material, Section C. Modeling of the argon nanofilm for details). The position of the surface of tension was calculated using the distribution of the pressure tensor components in the interfacial region, as presented in Figures S4 and S5). (see Supplementary Material, Section C.).

The calculated values of the equimolar surface position (Z_e) and the surface of tension (Z_s), along with the corresponding Tolman length (δ), are presented in Table S1. The results indicate that for the liquid-solid interface, the Tolman length is 5.5 ± 0.3 Å, whereas for the liquid-gas interface, it is 7.0 ± 0.5 Å. These values highlight the varying behavior of the surface tension correction across different interfaces.

Surface tension for the flat interfaces was calculated using Bakker's formula (9), which integrates the difference between the normal and tangential components of the pressure tensor across the interfacial region. The calculated surface tension values for the flat interfaces were found to be $\gamma_{ls} = 15.6 \pm 0.2$ mJ/m^2 for the liquid-solid interface and $\gamma_{lg} = 13.7 \pm 0.2$ mJ/m^2 for the liquid-gas interface. These results indicate that the surface tension is slightly higher at the liquid-solid interface compared to the liquid-gas interface.

For a comprehensive understanding of the simulation results, including the positions of equimolar and tension surfaces, as well as the calculated surface tension values, readers are referred to the supplementary material, which includes detailed graphs and tables (see Figs S2 – S9 and Table S1, in Supplementary Material, Section C. for details).

Modeling sessile droplets on surfaces of different wettability

The argon nanodroplets were modeled using the same potential (Eq. (13)) that was employed to simulate the substrate in the case of the nanofilm. Therefore, the temperature at the triple point of argon (83.8058 K) was selected, and the Gibbs canonical ensemble (NVT) was used. In cases where nanodroplets are modeled on a substrate composed of atoms of a different type, the methodology for adjusting the potential well depth of the interaction potential between the droplet molecules/atoms and the substrate can be applied as proposed in the works by Burian et al.[46,52]. The "cylindrical droplet" stabilization was achieved by establishing periodic boundary conditions (in the simulation box), i.e., through its infinite periodic extension along the cylinder axis.

Conducted simulations repetitions of cylindrical droplets of argon equals six for different sizes made of 2535, 5415, 10,935, 20,535, 36,015, 45,375 atoms, and even seven for the smallest configuration (1 215 atoms). In each case, in the initial configuration state, argon atoms were created (in the crystalline state) in part of the simulation box with dimensions of $6 \times 6 \times 15$, $9 \times 9 \times 15$, $13 \times 13 \times 15$, $18 \times 18 \times 15$, $24 \times 24 \times 15$, and $27 \times 27 \times 15$, respectively (defined in the parameters of the crystal lattice a_0). Schematic representations of thermalized configurations of two of them (the smallest and the largest) are shown in Fig. 2.

After the thermalization of each vapor-liquid systems, the calculation of two-dimensional maps of numerical density, Voronoi diagrams, and stress tensor components were performed every 1 ns by averaging 1000 similar values generated at every 100th calculation step. The total time of such averaging for some simulations lasted

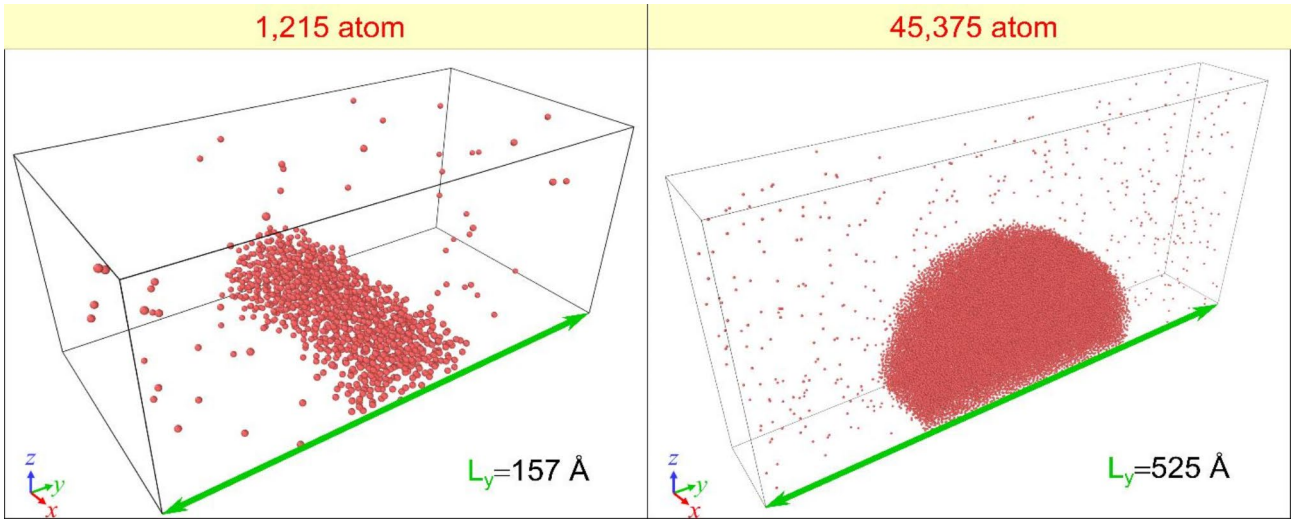

Fig. 2. Schematic representation of thermalized configuration (right and left in the upper part of the figure) of the cylindrical argon droplet for two different sizes and with different numbers of atoms.

for 13 ns. Each of the six nanodroplets was modeled on three substrates of different degrees of wettability. The degree of wettability was modeled by changing the depth of the potential well in the "potential model" (13) . Two-dimensional maps of those calculated quantities were constructed similarly to the case of the argon nanofilm. Figure 3 show maps of numerical density and the average pressure values for the smallest and largest nanodroplets from each series of calculations.

Calculation of contact angles for sessile argon nanodroplets

To simplify calculations, we assume that the equimolar surface and the surface of tension are equidistant and coaxial surfaces in the region where the density oscillations caused by the substrate field do not exceed the value of density fluctuation over the entire cross-section considered (see side inserts on the left in each graph of Fig. 3). For this part of the nanodroplet, the position of the equimolar surface was determined by approximating it with a circular arc, along which the values of the number density fall within the range [0.009; 0.011] $Å^{-3}$. It approximately corresponds to half liquid phase density. The radius of the nanodroplet surface is calculated by adding to the radius of the equimolar surface the value Tolman's δ. The interfaces of the fluid-solid contact are flat, so their position is easily determined by Eqs (6) and (11), and the magnitude of the Tolman length for the respective dividing boundary is calculated according to expression (12).

Using Eq. (6) and (11) one can calculate the positions of the flat equimolar dividing surface and the surface of tension, just as demonstrated in the previous section for the argon nanofilm. Fig. S6 (see Supplementary Material, Section C.) shows the arithmetic area under the curve at the solid substrate-liquid dividing boundary, giving the value of the respective component of the surface tension tensor, just as in the case of the liquid-gas boundary. Using the obtained values of the positions of the dividing surfaces by formula (12), the value of the Tolman length $\delta = 7.0 \pm 1.8$ Å was calculated. The positive value of the value δ, the Tolman length, means that the surface of tension is at a distance of 7 Å from the equimolar dividing surface in the direction of the fluid, which is consistent with known literature results. For all three series of MD calculations, it was established that the surface of tension at the liquid-substrate boundary is closer to the liquid phase by approximately 5.5 ± 0.7 Å, than the corresponding equimolar surface.

For the cylindrical nanodroplet, analyzing the narrow region near the axial section perpendicular to the base of the droplet (see examples in Fig. 4), similar calculations were made as for the nanofilm. The value of the Tolman length within the margin of error is the same as the one obtained for the liquid-gas interface of the nanofilm.

As seen in Fig. 5, the WCA calculated as dihedral angles between the equimolar surfaces at the liquid-gas and liquid-solid boundaries and the respective surfaces of tension, for the droplet of the smallest radius (11.8 ± 0.4 Å) in the second series of simulations, turn out to be different, namely, equal to $79.5^o \pm 2.7^o$ and $100.2^o \pm 2.1^o$ respectively (for droplets of all sizes see Figs. 6 and 7 and Figs S10, S11 in supplementary material).

The over 10% discrepancies between the contact angles determined for the equimolar surface and the surface of tension reflect fundamental differences between these two approaches. The equimolar surface defines the geometric phase boundary where the number of particles on both sides is equal, making it useful for describing the spatial characteristics and shape of the droplet. In contrast, the surface of tension is a thermodynamically defined boundary that ensures the equilibrium of interfacial forces, making it more relevant for analyzing interfacial energy interactions and mechanical equilibrium in the system.

These discrepancies indicate that both approaches capture different physical aspects of wetting. For studies focusing on droplet shape and geometry, the equimolar surface is preferable. However, for analyzing wetting in the context of thermodynamic equilibrium between phases, the surface of tension provides a more accurate representation. Both methods are valuable, depending on the research objectives.

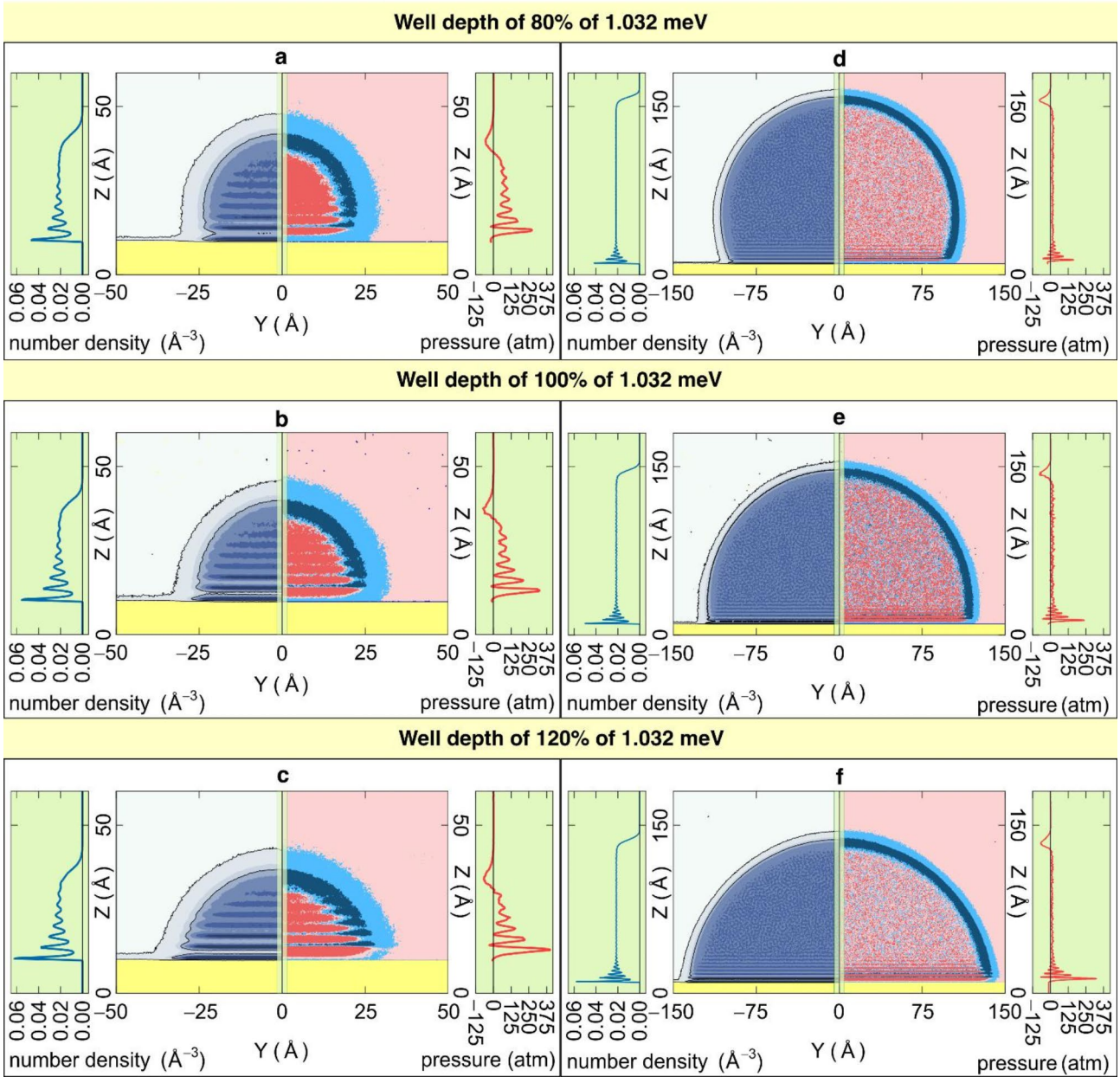

Fig. 3. Maps of averaged distributions of numerical density (left) and pressure (right) along the axis of cylindrical argon droplets. Panels (**a**), (**b**), and (**c**) depict the smallest droplet in the series (2535 atoms), while panels (**d**), (**e**), and (**f**) illustrate the largest droplet (45375 atoms). The left side insets in each panel show the variation of numerical density along the Z-axis (height) of the droplet, indicating how the density distribution changes from the base to the top of the droplet. The right side insets display the corresponding pressure profiles, showing the variation of pressure across the Z-axis, which helps in understanding the stress distribution within the droplet. Panels (**a**, **d**), (**b**, **e**), and (**c**, **f**) correspond to potential well depths of 80%, 100%, and 120% of 1.032 meV, respectively, representing the corresponding levels of substrate wettability.

The fluctuation character of the distribution of contact angle values (see Fig. S11 in supplementary material), calculated every 1 ns for each droplet in all series of MD simulations, provides a justified basis for averaging such values among all droplets across all series of calculations (refer to Fig. S10 and Fig. S11 in supplementary material Section D. Analysis of random fluctuations in contact angle during simulation).

Considering that the thickness of the interfacial region remains nearly constant with the change in the curvature of the interface, the difference in contact angles measured between the stretching surfaces and equimolar dividing surfaces increases with the decrease in the cross-section of the nanodroplet. In each case, for the contact angles determined between the equimolar surfaces and even more so for the contact angles determined between the tension surfaces, these contact angles are dependent on the cylindrical droplet is cross-sectional size (see Figs. 6, 7 and 8).

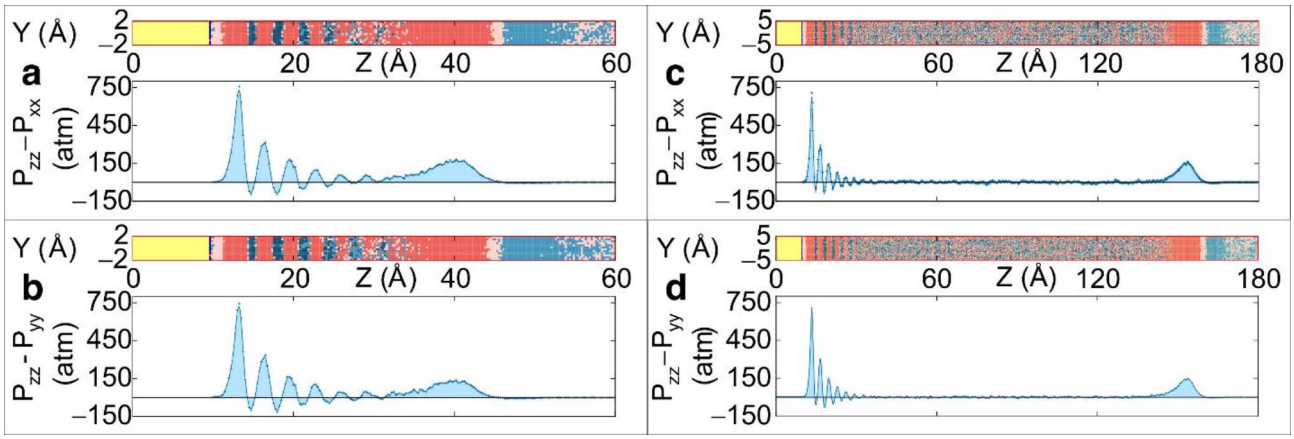

Fig. 4. MD calculation results of the difference between the normal and tangential components of the pressure tensor, in the *x* and *y* directions, tangent to the narrow part of the surface of the smallest (**a** and **b**) and largest droplets (**c** and **d**), respectively.

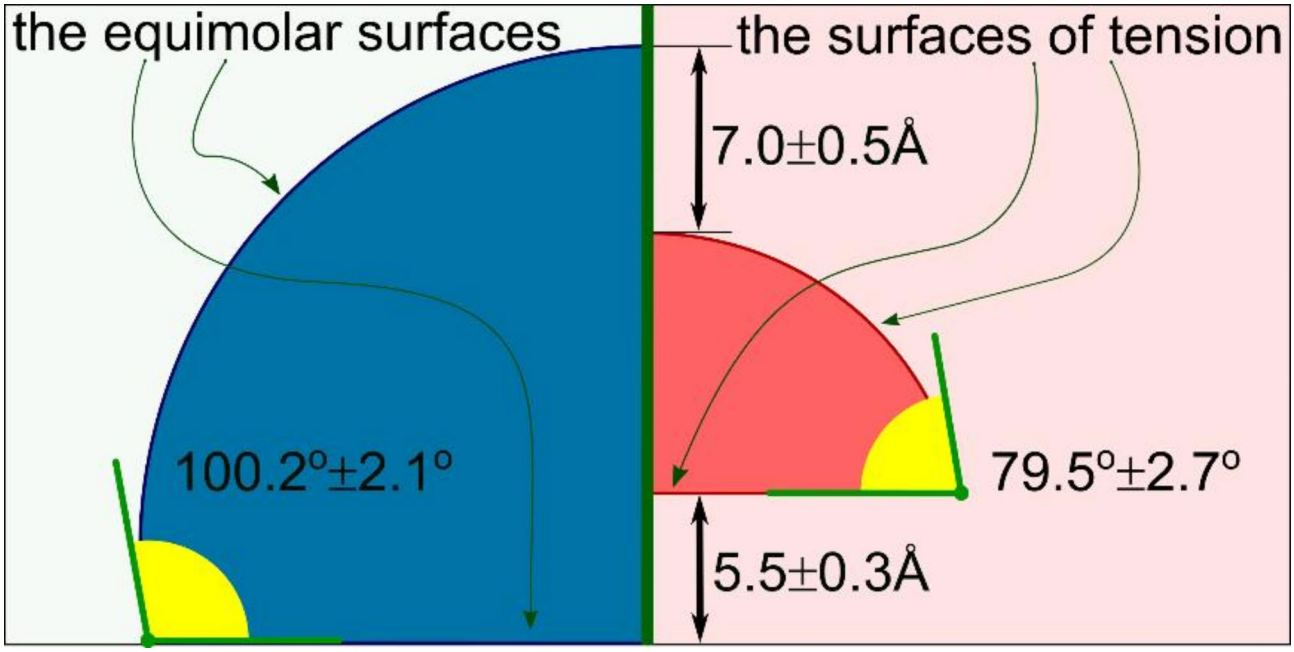

Fig. 5. Schematically shown are the positions of the equimolar surfaces, constructed using the Gibbs method (left) in the reference system and the corresponding surfaces of tension (right) in the case of the smallest nanodroplet in the second series of calculations (1215 atoms). The distances between the respective dividing surfaces and the angles between them are indicated.

Within the Gibbs-Tolman method, it is known that the size dependence of the surface tension of a spherical droplet or a bubble is described by the Tolman approximation[8,9], and for the case of cylindrical phase boundaries, the size dependence of the surface tension is described by a modified expression given in the work[21]

$$\gamma_{lg}(R) = \frac{\gamma_{lg}^{\infty}}{1+\delta/R}, \tag{14}$$

where $\gamma_{lg}(R)$ is the surface tension for a droplet with radius R, γ_{lg}^{∞} is the surface tension for a flat surface, and the Tolman length δ. Using Young's equation for the macroscopic contact angle (θ) at the three-phase boundary (liquid, solid, and gas):

$$\gamma_{lg}\cos(\theta) = \gamma_{sg} - \gamma_{sl}, \tag{15}$$

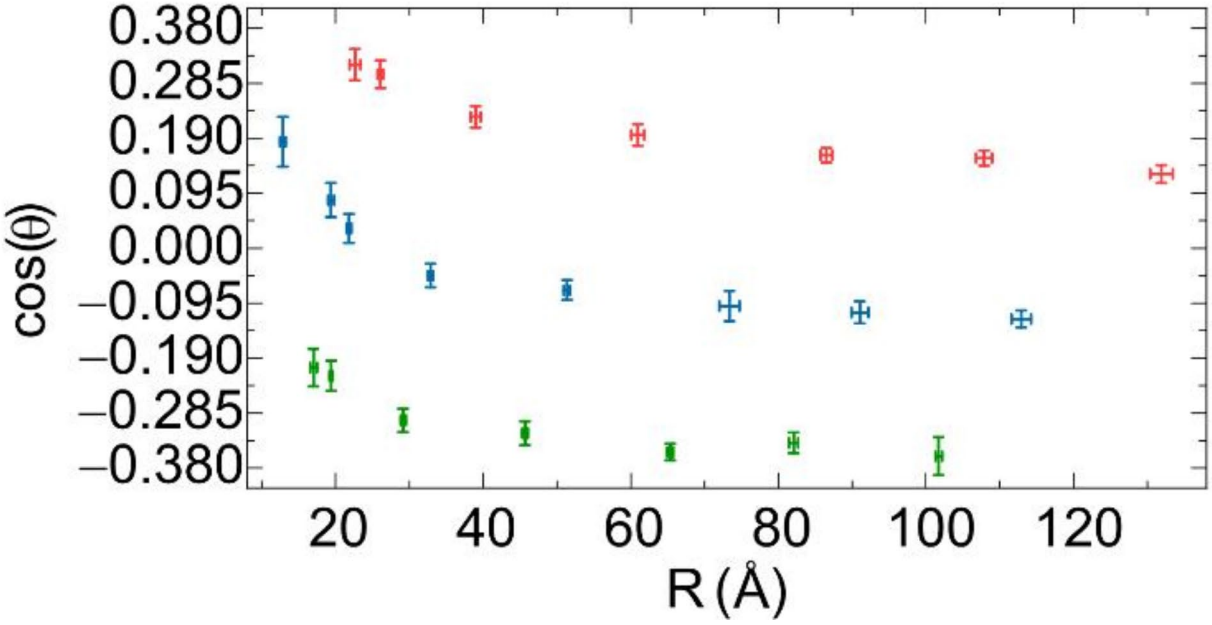

Fig. 6. The values of the cosine of the contact angle for sessile nanodroplets with different radii of the surface of tension. The angles are calculated between the surfaces of tension.

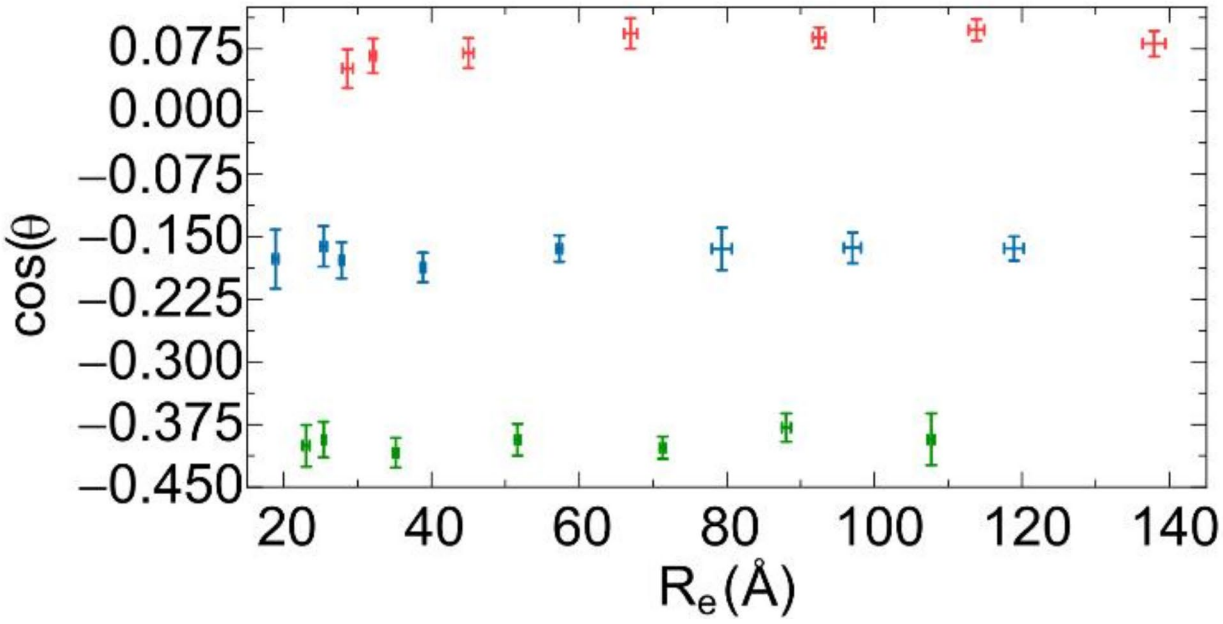

Fig. 7. The values of the cosine of the contact angle for sessile nanodroplets with different radii of the equimolar surface. The angles are calculated between the equimolar surfaces.

where γ_{sg} is the surface tension between the solid and gas, γ_{sl} is the surface tension between the solid and liquid, and γ_{lg} is the surface tension between the liquid and gas. Considering the modified Tolman approximation (14), Young's equation can be modified for nanoscale droplets by accounting for the size-dependent surface tension

$$\cos(\theta) = \cos(\theta_{\text{Young}})(1 + \delta/R), \tag{16}$$

where θ_{Young} is the macroscopic contact angle. This expression shows that the contact angle at the nanoscale depends on the Tolman length δ and the radius R of the droplet. Using this equation as an approximation

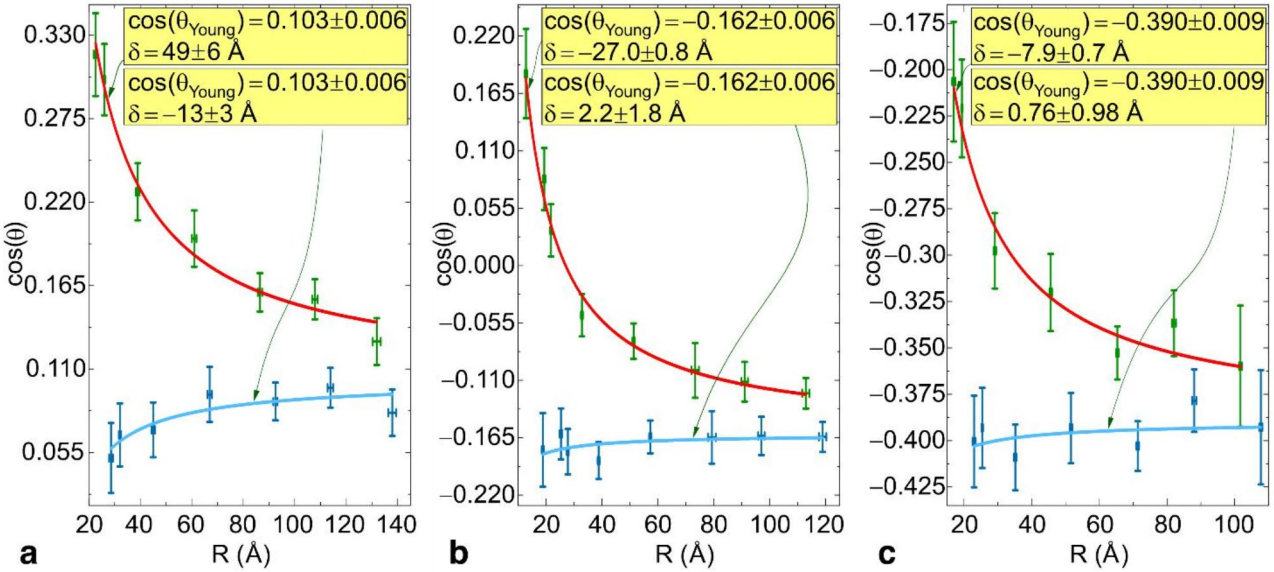

Fig. 8. Dependence of the cosine of the contact angle cos(θ) on the droplet radius R with approximations (16) for different Tolman length values δ. Green points: cosine values of contact angles versus the radius of the surface of tension. Blue points: cosine values of contact angles versus the radius of the equimolar dividing surface. (**a**) Red curve: approximation according to the model with $\delta = 41 \pm 4$ Å. Blue curve: approximation according to the model with $\delta = -17 \pm 2$ Å. The value of $\cos(\theta_{Young})$ for both curves is 0.108 ± 0.005. (**b**) Red curve: approximation according to the model with $\delta = -24.8 \pm 0.8$ Å. Blue curve: approximation according to the model with $\delta = 2.2 \pm 1.7$ Å. The value of $\cos(\theta_{Young})$ is -0.162 ± 0.006 for the red curve and -0.162 ± 0.007 for the blue curve. (**c**) Red curve: approximation according to the model with $\delta = -6.9 \pm 0.5$ Å. Blue curve: approximation according to the model with $\delta = -0.4 \pm 0.7$ Å. The value of $\cos(\theta_{Young})$ for both curves is -0.399 ± 0.007.

model, the contact angle for nanodroplets of various sizes can be estimated. The derived expression is used to approximate the results presented in the graphs (see Fig. 8). This allows the assessment of the impact of nanoscale effects on the contact angle and the consistency of the results with theoretical predictions.

However, the values of the Tolman length obtained as a fitting parameter for this model based on simulation data do not match the values of the Tolman length calculated as the distance from the equimolar surface to the surface of tension in the case of a flat interface. This discrepancy indicates that a model accounting solely for the size dependence of surface tension needs to be revised to accurately describe the obtained data.

It is obvious that additional effects, not solely related to the size dependence of surface tension, need to be considered. For instance, the presence of other surface phenomena, such as line tension or the influence of molecular structure at the phase boundary, could be a potential cause of these discrepancies.

Conclusions.

In nanoscale multiphase systems, the ambiguity in defining the location of an interface is related to the interfacial layer (interphase transition region), which has a thickness on the order of the characteristic linear dimensions of the system itself. Such difficulty is often the reason to explain the uncertainty in determining wetting contact angles which are key parameters for understanding wetting phenomena. This study highlights the importance of selecting an appropriate dividing surface at the nanoscale for accurately describing the wetting behavior. The Gibbs dividing surface method provides a mechanically equivalent representation to the natural physical system and allows accurate determination of the contact angle as the dihedral angle at the three-phase line of tension between the tangents to the respective tension surfaces.

The positions of the Gibbs surfaces were determined using MD simulations of cylindrical argon nanodroplets and nanofilms. The Tolman length, determined at the triple point temperature of argon, was approximately 8 Å, corresponding to about a quarter of the surface tension radius for the nanodroplets. This study also allowed the calculation of contact angles, defined both between the equimolar surfaces and between the tension surfaces for the cylindrical nanodroplet, which were $88.9 \pm 0.3°$ and $101.3 \pm 0.2°$, respectively. These results contribute to a better understanding of wetting dynamics at the nanoscale and illustrate the complex aspects associated with interpreting contact angles in such small systems.

Considering droplets of different sizes, a dependence of the wetting contact angles, both between equimolar surfaces and tension surfaces, on the cross-section radius of the cylindrical droplet with a straight three-phase contact line was found. However, the nature of the size dependence of the contact angle cannot be solely related to the size dependence of surface tension within the Tolman approximation. This dependence may be caused by the presence of line tension or adsorption. It was established that the differences in the contact angle values between equimolar surfaces and tension surfaces increase with decreasing cross-sectional radius of the nanodroplet and become negligible for macroscopic sizes.

From an experimental perspective, the observed differences between contact angles measured for equimolar surfaces and surfaces of tension may depend on the measurement technique. For instance, scanning electron microscopy (SEM), which generates density maps, would capture the wetting angle based on the equimolar surface, reflecting the droplet's geometric properties. In contrast, atomic force microscopy (AFM), which probes interfacial forces, would measure wetting characteristics based on the surface of tension, focusing on the thermodynamic equilibrium of the system. This distinction highlights the importance of considering the features of the experimental approach when interpreting wetting phenomena at the nanoscale.

Data availability

All data generated from the molecular dynamics simulations and analyzed during this study will be available upon reasonable request to the primary corresponding author, Burian Sergii (burian_sergii@knu.ua).

Received: 6 September 2024; Accepted: 9 December 2024
Published online: 28 December 2024

References

1. Daniel, D. et al. Probing surface wetting across multiple force, length and time scales. *Commun. Phys.* **6**, 152 (2023).
2. Drelich, J. W. et al. Contact angles: history of over 200 years of open questions. *Surf. Innov.* **8**, 3–27 (2020).
3. Mandrolko, V. et al. Features of the contact angle hysteresis at the nanoscale: a molecular dynamics insight. *Phys. Fluids*. **36**, 52012 (2024).
4. Klauser, W., von Kleist-Retzow, F. T. & Fatikow, S. Line tension and Drop size dependence of Contact Angle at the Nanoscale. *Nanomaterials* **12**, 369 (2022).
5. Gong, S., Hu, Z., Dong, L. & Cheng, P. Temperature- and curvature-dependent surface tensions and Tolman lengths for real fluids: a mesoscopic investigation. *Phys. Fluids* **35**, (2023).
6. Tan, B. H., An, H. & Ohl, C. D. Body forces drive the Apparent Line Tension of Sessile droplets. *Phys. Rev. Lett.* **130**, 064003 (2023).
7. Lei, Y. A., Bykov, T., Yoo, S. & Zeng, X. C. The Tolman length: is it positive or negative? *J. Am. Chem. Soc.* **127**, 15346–15347 (2005).
8. Tolman, R. C. The Effect of Droplet size on Surface Tension. *J. Chem. Phys.* **17**, 333–337 (1949).
9. Kirkwood, J. G. & Buff, F. The statistical mechanical theory of surface tension. *J. Chem. Phys.* **17**, 338–343 (1949).
10. Rowlinson, J. S. & Widom, B. Molecular theory of capillarity. *Dover Publications Inc*. https://doi.org/10.1016/0368-1874(84)87080-X (1982).
11. Ono, S. & Kondo, S. Molecular Theory of Surface Tension in liquids. *Struct. Liq / Strukt Der Flüssigkeiten*. **255**, 134–280 (1960).
12. Hemingway, S. J., Henderson, J. R. & Rowlinson, J. S. The density profile and surface tension of a drop. *Faraday Symp. Chem. Soc.* **16**, 33 (1981).
13. Guermeur, R., Biquard, F. & Jacolin, C. Density profiles and surface tension of spherical interfaces. Numerical results for nitrogen drops and bubbles. *J. Chem. Phys.* **82**, 2040–2051 (1985).
14. Horsch, M. et al. Excess equimolar radius of liquid drops. *Phys. Rev. E.* **85**, 031605 (2012).
15. Iwamatsu, M. The surface tension and Tolman's length of a drop. *J. Phys. Condens. Matter*. **6**, L173–L177 (1994).
16. Blokhuis, E. M. & Kuipers, J. Thermodynamic expressions for the Tolman length. *J. Chem. Phys.* **124**, 074701 (2006).
17. Azouzi, M. E. M., Ramboz, C., Lenain, J. F. & Caupin, F. A coherent picture of water at extreme negative pressure. *Nat. Phys.* **9**, 38–41 (2012).
18. Joswiak, M. N., Duff, N., Doherty, M. F. & Peters, B. Size-dependent surface Free Energy and Tolman-Corrected Droplet Nucleation of TIP4P/2005 water. *J. Phys. Chem. Lett.* **4**, 4267–4272 (2013).
19. Joswiak, M. N., Do, R., Doherty, M. F. & Peters, B. Energetic and entropic components of the Tolman length for mW and TIP4P/2005 water nanodroplets. *J. Chem. Phys.* **145**, 204703 (2016).
20. Wilhelmsen, Ø., Bedeaux, D. & Reguera, D. Tolman length and rigidity constants of the Lennard-Jones fluid. *J. Chem. Phys.* **142**, 064706 (2015).
21. Burian, S., Isaiev, M., Termentzidis, K., Sysoev, V. & Bulavin, L. Size dependence of the surface tension of a free surface of an isotropic fluid. *Phys. Rev. E*. **95**, 062801 (2017).
22. Gurkov, T. D. & Kralchevsky, P. A. Surface tension and surface energy of curved interfaces and membranes. *Colloids Surf.* **47**, 45–68 (1990).
23. Marmur, A. Soft contact: measurement and interpretation of contact angles. *Soft Matter*. **2**, 12–17 (2006).
24. Herrmann, H. & Bucksch, H. contact angle α. in *Dictionary Geotechnical Engineering/Wörterbuch GeoTechnik* vol. 577 284–284Springer Berlin Heidelberg, (2014).
25. Marmur, A., Della Volpe, C., Siboni, S., Amirfazli, A. & Drelich, J. W. Contact angles and wettability: towards common and accurate terminology. *Surf. Innov.* **5**, 3–8 (2017).
26. Láng, G. G. Basic interfacial thermodynamics and related mathematical background. *ChemTexts* **1**, 16 (2015).
27. Adamson, A. W. *Physical Chemistry of Surfaces* (A Wiley-Interscience Publication, 1997).
28. Werder, T., Walther, J. H., Jaffe, R. L., Halicioglu, T. & Koumoutsakos, P. On the Water–Carbon Interaction for Use in Molecular Dynamics simulations of Graphite and Carbon Nanotubes. *J. Phys. Chem. B*. **107**, 1345–1352 (2003).
29. Weijs, J. H., Marchand, A., Andreotti, B., Lohse, D. & Snoeijer, J. H. Origin of line tension for a Lennard-Jones nanodroplet. *Phys. Fluids*. **23**, 022001 (2011).
30. Hong-Kai, G. & Hai-Ping, F. Drop size dependence of the Contact Angle of Nanodroplets. *Chin. Phys. Lett.* **22**, 787–790 (2005).
31. Ingebrigtsen, T. & Toxvaerd, S. Contact angles of Lennard-Jones liquids and droplets on planar surfaces. *J. Phys. Chem. C.* **111**, 8518–8523 (2007).
32. Peng, H., Birkett, G. R. & Nguyen, A. V. The impact of line tension on the contact angle of nanodroplets. *Mol. Simul.* **40**, 934–941 (2014).
33. Yamaguchi, Y., Kusudo, H., Surblys, D., Omori, T. & Kikugawa, G. Interpretation of Young's equation for a liquid droplet on a flat and smooth solid surface: mechanical and thermodynamic routes with a simple Lennard-Jones liquid. *J. Chem. Phys.* **150**, 044701 (2019).
34. Kralchevsky, P. A. & Nagayama, K. Interfaces of Moderate Curvature: Theory of Capillarity. in *Studies in Interface Science* vol. 10 64–104 (2001).
35. Kralchevsky, P. A., Eriksson, J. C. & Ljunggren, S. Theory of curved interfaces and membranes: mechanical and thermodynamical approaches. *Adv. Colloid Interface Sci.* **48**, 19–59 (1994).
36. Ljunggren, S., Eriksson, J. C. & Kralchevsky, P. A. Minimization of the Free Energy of arbitrarily curved interfaces. *J. Colloid Interface Sci.* **191**, 424–441 (1997).
37. Mahnke, R. & Schmelzer, J. A. New General Formula for the curvature dependence of Surface Tension of droplets. *Z. für Phys. Chemie*. **266**, 1028–1031 (1985).

38. Schmelzer, J. W. P., Gutzow, I. & Schmelzer, J. Curvature-dependent surface tension and nucleation theory. *J. Colloid Interface Sci.* **178**, 657–665 (1996).
39. Schmelzer, J. The curvature dependence of surface tension of small droplets. *J. Chem. Soc. Faraday Trans. 1 Phys. Chem. Condens. Phases*. **82**, 1421 (1986).
40. Pasandideh-Fard, M., Chen, P., Mostaghimi, J. & Neumann, A. W. The generalized Laplace equation of capillarity I. Thermodynamic and hydrostatic considerations of the fundamental equation for interfaces. *Adv. Colloid Interface Sci.* **63**, 151–177 (1996).
41. Kralchevsky, P. A., Gurkov, T. D. & Ivanov, I. B. The interfacial bending moment: thermodynamics and contributions of the electrostatic interactions. *Colloids Surf.* **56**, 149–176 (1991).
42. Kralchevsky, P. A. Micromechanical description of curved interfaces, thin films, and membranes. *J. Colloid Interface Sci.* **137**, 217–233 (1990).
43. Kralchevsky, P. A. & Nagayama, K. *Particles at Fluid Interfaces and Membranes Attachment of Colloid Particles and Proteins to Interfaces*. *Interface Science* vol. 10Elsevier Science, (2001).
44. Desgranges, C. & Delhommelle, J. Evaluation of the grand-canonical partition function using expanded Wang-Landau simulations. III. Impact of combining rules on mixtures properties. *J. Chem. Phys.* **140**, (2014).
45. Delhommelle, J. & Millié, P. Inadequacy of the Lorentz-Berthelot combining rules for accurate predictions of equilibrium properties by molecular simulation. *Mol. Phys.* **99**, 619–625 (2001).
46. Isaiev, M. et al. Efficient tuning of potential parameters for liquid–solid interactions. *Mol. Simul.* **42**, 910–915 (2016).
47. Thompson, A. P. et al. LAMMPS - a flexible simulation tool for particle-based materials modeling at the atomic, meso, and continuum scales. *Comput. Phys. Commun.* **271**, 108171 (2022).
48. Saville, G. Computer simulation of the liquid–solid–vapour contact angle. *J. Chem. Soc. Faraday Trans. 2*. **73**, 1122–1132 (1977).
49. Toxvaerd, S. Molecular dynamics simulation of heterogeneous nucleation at a structureless solid surface. *J. Chem. Phys.* **117**, 10303–10310 (2002).
50. De Groot, S. R. & Mazur, P. *Non-Equilibrium Thermodynamics* (Dover, 2013).
51. Thompson, A. P., Plimpton, S. J. & Mattson, W. General formulation of pressure and stress tensor for arbitrary many-body interaction potentials under periodic boundary conditions. *J. Chem. Phys.* **131**, (2009).
52. Aleksandrovych, M. et al. Effect of Surface Nano-Texturing on Wetting properties: Molecular Dynamics Study. *Ukr. J. Phys.* **65**, 817 (2020).

Acknowledgements

This research was supported by the ANR project "PROMENADE" No. ANR-23-CE50-0008, as well as by the European Commission within the scope of FP Horizon 2020 (Project "EHAWEDRY", Grant Agreement No. 964524). Molecular simulations were conducted using HPC resources from GENCI-TGCC and GENCI-IDRIS (No. A0150913052).

Author contributions

CRediT Author Statement: BS: Writing - Original Draft, Methodology, Formal Analysis, Investigation; BS and MI: Conceptualization; YS and BS: Visualization, Software; AY and MI: Funding Acquisition, Methodology, Writing - Review & Editing; LB: Methodology, Writing - Review & Editing; DL and MI: Resources, Writing - Review & Editing; MI: Resources, Data Curation, Supervision, Project Administration.All authors have reviewed and approved the final version of the manuscript.

Declarations

Competing interests

The authors declare no competing interests.

Additional information

Supplementary Information The online version contains supplementary material available at https://doi.org/10.1038/s41598-024-82683-2.

Correspondence and requests for materials should be addressed to S.B.